Post-Print

This is the accepted version of:

Aeroelastic Analysis of a Cycloidal Rotor Under Various Operating Conditions

Louis Gagnon,* Marco Morandini,† Giuseppe Quaranta,‡ Pierangelo Masarati§

Politecnico di Milano, Milano, 20156, Italy

Carlos M. Xisto,¶

Chalmers University of Technology, 41296, Göteborg, Sweden

José C. Páscoa‖

Universidade da Beira Interior, Covilhã, Portugal

The aeroelasticity of a cycloidal rotor in forward flight is investigated using an analytical and a numerical model, the latter is based on a multibody dynamics approach. Three experimental sources are used to validate the multibody model. The influence of the number of blades, their stiffness, and skin thickness are investigated. At high pitch angles, before stall and flexibility effects occur, increasing the number of blades produces more thrust for the same power. Flexibility and skin thickness considerably affect the required pivot rod strength and blade deformation. Simply supported blades exhibit severe deformations when compared to clamped blades. Thrust and power are both influenced in a similar and moderate way by flexibility. The rotor response to wind gusts is also analyzed. The

---

*Postdoctoral Research Fellow, Department of Aerospace Science and Technology, via La Masa 34, louis.gagnon@polimi.it

†Associate Professor, Department of Aerospace Science and Technology, via La Masa 34, marco.morandini@polimi.it

‡Associate Professor, Department of Aerospace Science and Technology, via La Masa 34, giuseppe.quaranta@polimi.it

§Associate Professor, Department of Aerospace Science and Technology, via La Masa 34, pierangelo.masarati@polimi.it, AIAA Member

¶Researcher, Department of Mechanics and Maritime Sciences, Division of Fluid Dynamics, carlos.xisto@chalmers.se

‖Associate Professor, C-MAST, Dep. de Eng. Electromecânica, Rua Mq.s D'Ávila e Bolama, 6201-001 Covilhã, pascoa@ubi.pt

angular velocity of the rotor significantly affects the response of the rotor to wind gusts. The direction of the gusting wind has an important influence on power, whereas thrust increases regardless of wind direction. Finally, the rotor response lags minimally behind the arrival of the gust.

I.   Introduction

The first records for a cycloidal rotor date from 1923 when a Canadian self-taught aeronautical engineer, Jonathan Edward Caldwell, filed for a patent concerning a cyclogyro[a]. This airplane would have been propelled by cycloidal rotors. Unfortunately, Caldwell was never able to actually fly the machine and the project was left aside. The cycloidal rotor was also conceived in a patent by Herbert M. Heuver in 1936 [1] and again near the end of the second world war when Heuver filed a patent [2] for an improved blade pitching mechanism. These projects did not lead to further developments.

Cycloidal rotors are also a viable means to transform the kinetic energy of an airflow into mechanical energy which is gathered by applying a resistive torque to the rotor shaft. This is the case of the Darrieus lift-based vertical axis wind turbine which owes its name to its inventor [3]. This paper rather focuses on the ability of cycloidal rotors to produce aerodynamic forces whose direction can be rapidly varied in a plane normal to the axis of rotation. Today, several such applications of the cycloidal rotor principle exist. An example is the Voith Schneider marine propulsion system. It is used in tow and ferry boats precisely because of its ability to quickly direct thrust in a desired direction [4]. In the aeronautical field, the cyclogyro concept has been recently investigated and improved. Kim *et al.* [5] report using carbon fiber blades and a testing apparatus which allows to easily test different rotor radii. Their studies were directed at increasing the thrust to power ratio of the cycloidal rotor. Siegel *et al.* [6] studied the low-Reynolds behavior of the cycloidal rotor. Their need to reproduce the wing motions found in nature while still using an engine and a shaft to transmit power justifies their use of a cycloidal rotor. The MAAT project [7] and Bosch Aerospace [8] also proposed the rotor as a means of propulsion for airships. One great advantage they find to such rotors is that they provide excellent control during takeoff and landing. Such maneuvers are not possible with typical control surfaces which rely on air flow. Its use as a means to produce lift, thrust and control forces has also been studied for other types of air vehicles such as micro-aerial vehicles (MAV) in the United States [9–13]. Recently in the Northwestern Polytechnical University of China [14, 15] developed an unmanned cycloidal rotor aircraft which uses two such rotors accompanied by a small conventional rotor at the tail. An analogous configuration has also been extensively studied and flown by the

---

[a]http://www.aerofiles.com/graygoose.html, last accessed March 2018.

University of Maryland [16,17]. With its vertically directed axis, that tail rotor counters the torque created by the cycloidal rotors about the pitch axis and increases the lift capability. They were able to fly the MAV in forward flight at constant altitude using their own control system. Other recent advances include a patent filed in 2011 by Eurocopter [18], in which a cycloidal rotor is embed in the tail boom of a helicopter. The rotor has its axis along the boom itself and acts as an anti-torque device to replace the conventional helicopter tail rotor. The Austrian company IAT21 currently works at the D-Dalus project[b], which uses the cyclorotor concept for the lift, propulsion, and control of a manned vehicle. Figure 1 shows the unmanned concept aircraft technology.

Figure 1. The D-Dalus concept developed by IAT21.

Figure 2 illustrates the working principle of cycloidal rotors. A drum carries a set of wings, or blades, whose axes are aligned with the rotation axis of the drum. In the figure, the blue pivot rods are connected to the pivoting point of the blades, which always remains at an equal distance from the rotation center. Each blade can pitch about a feathering axis which is also aligned with the rotation axis of the drum. By periodically pitching the blades with a period equal to that of the drum rotation. Thus, a net aerodynamic force normal to the rotation axis is generated. The amplitude and the direction of the pitch can be controlled by relatively simple mechanical arrangements. One such arrangement is shown by the green pitch control rods of Fig. 2 which rotate with the principal drum but have an offset center of rotation.

The amplitude of the periodic pitch is often fixed. In such cases, the thrust magnitude is controlled by changing the rotor angular velocity. The possibility to use independent blade pitch control promises performance improvements, as shown by [19] for water turbines. This broadens the applicability of the concept.

The need for aeroelasticity in the investigation of cyclogyro dynamics is highlighted in Figure 3, which presents a detail of a MAV-scale cyclogyro blade during normal operation when subjected to aerodynamic and inertia loads, as discussed in [12]. Inertia usually plays a dominant role. The blade undergoes such a significant deformation that the local angle of

---

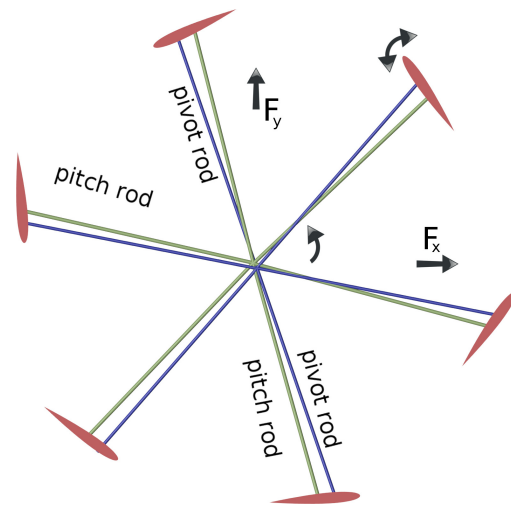[b]http://iat21.at/, last accessed Feb 2015.

Figure 2. Sketch of cycloidal rotor working principle.
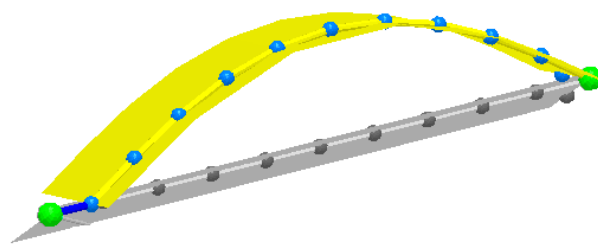

Figure 3. Deformation of a cycloidal rotor blade subjected to inertial and aerodynamic loads.

attack may be drastically modified.

The capability of the relatively simple but effective aeroelastic formulation considered in this work for blade flexibility is proved by the results originally presented in [12], which were related to MAV-scale experimental results obtained with monolithic blades of different geometry.

In 2013-2014, the European Commission sponsored the Cycloidal Rotor Optimized for Propulsion (CROP) project[c]. This consortium aimed at evaluating possible improvements to the cyclogyro concept including optimized pitching schedules; electrohydrodynamic actuation to maintain an attached boundary layer at high pitch; better three-dimensional flow control; and, the evaluation of aeroelastic behavior of the rotor. The present work addresses the investigations carried on about the aeroelasticity of cycloidal rotors. The aeroelastic analysis is mainly performed using the free general-purpose multibody analysis software MBDyn[d], which is developed at the Department of Aerospace Science and Technology of Politecnico di Milano. In this paper, analytic considerations are first presented and are followed by a multibody model which is validated trough a comparison with three different experiments. The multibody model is used to study the impact of wind gusts, material rigidity, and skin thickness on the fixed cycloidal rotor.

II. Analytical aeroelastic model

This section presents some considerations on the aeroelasticity of the cycloidal rotor arrangement. Low-solidity rotor designs were shown to have an aerodynamic efficiency advantage [20] for rotors in the size range of manned aircraft. In the case of micro air vehicles, the tendency is inverted [21]. In this paper, the influence of solidity was analyzed prior to carrying on with a geometry proposed by Yun *et al.* [22]. Cycloidal rotors are characterized by very slender blades and low torsional stiffness. The shear, mass, and aerodynamic centers of the blade section are also offset from the pitch axis. All this may become problematic when considering the elastic behavior of such a rotor.

Figure 4 shows a sketch of the blade section where x_a is the distance of the aerodynamic center from the pitch axis; x_e is the distance of the elastic axis from the pitch axis; and, x_m is the distance of the center of mass from the pitch axis.

The blades are mainly loaded by nearly radial out-of-plane centrifugal and aerodynamic forces. The latter may show a significant tangential component when operating at high pitch

---

[c]http://crop.ubi.pt/, last accessed March 2018.
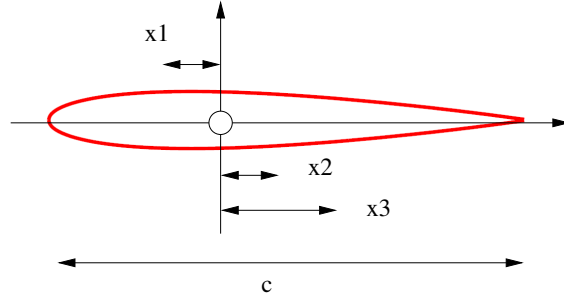[d]http://www.mbdyn.org/, last accessed February 2015.

Figure 4. Sketch of blade section.

magnitude. The force per unit span is

$$f_{\text{radial}} = f_c + f_a \approx m\Omega^2 r + \frac{1}{2}\rho(\Omega r)^2 c C_L, \tag{1}$$

where m is the blade mass per unit span; f_c and f_a are the radial contributions of the centrifugal and aerodynamic loads, respectively; and r is the distance from the rotation center that includes the effect of deformation, i.e.

$$r(x,t) = R + w(x,t) \tag{2}$$

Thus, both loads are proportional to Ω^2 and to either r or r^2.
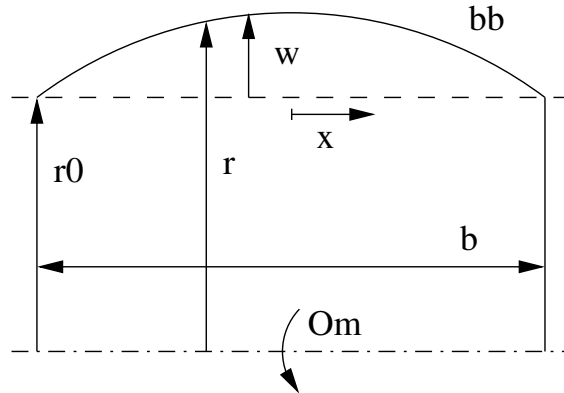

Figure 5. Schematic of rotating flexible blade assembly subjected to bending.

It is assumed that the blade is simply supported at both ends, as sketched in Fig. 5. Thrust and power coefficients are defined respectively as,

$$C_T = \frac{T}{\rho(\Omega R)^2 A} \tag{3}$$

and

$$C_P = \frac{P}{\rho(\Omega R)^3 A} \tag{4}$$

A. Static aeroelastic corrections

Consider the Euler-Bernoulli model for beam deflection in radial direction. A steady solution is sought, thus $\ddot{w} = 0$. All axes are assumed to be coincident with the pitch axis to simplify the analysis ($x_a = x_e = x_m = 0$). The virtual work principle yields

$$\int_{-b/2}^{b/2} \delta w'' E J w'' \, dx = \int_{-b/2}^{b/2} \delta w \, (f_c + f_a) \, dx \tag{5}$$

The bending displacement of the blade is approximated using a single shape function. This function is taken as the analytical solution of the first bending mode of a simply supported uniform beam,

$$w(x,t) \approx \cos\left(\frac{\pi}{b}x\right) q_w(t) \tag{6}$$

defined over the domain $x \in [-b/2, b/2]$,

$$\delta q_w \int_{-b/2}^{b/2} E J \left(\frac{\pi}{b}\right)^4 \cos^2\left(\frac{\pi}{b}x\right) \, dx \, q_w = \delta q_w \left\{ \int_{-b/2}^{b/2} \cos\left(\frac{\pi}{b}x\right) m\Omega^2 \left[R + \cos\left(\frac{\pi}{b}x\right) q_w\right] \, dx \right.$$
$$\left. + \int_{-b/2}^{b/2} \cos\left(\frac{\pi}{b}x\right) \frac{1}{2}\rho\Omega^2 c C_L \left[R^2 + 2R\cos\left(\frac{\pi}{b}x\right) q_w + \cos^2\left(\frac{\pi}{b}x\right) q_w^2\right] \, dx \right\} \tag{7}$$

i.e.

$$\frac{\pi^4}{2}\frac{EJ}{b^3} q_w = m\Omega^2 bR\left(\frac{2}{\pi} + \frac{1}{2}\frac{q_w}{R}\right) + \frac{1}{2}\rho\Omega^2 c C_L bR^2\left[\frac{2}{\pi} + \frac{q_w}{R} + \frac{4}{3\pi}\left(\frac{q_w}{R}\right)^2\right] \tag{8}$$

The problem can be solved analytically since it is quadratic in q_w. However, for realistic designs, it can be simplified further, neglecting the second-order term, $(q_w/R)^2$, under the assumption that $|q_w/R| \ll 1$. Thus,

$$\left[\frac{\pi^4}{2}\frac{EJ}{b^3} - \Omega^2 b\left(\frac{1}{2}m + \frac{1}{2}\rho c C_L R\right)\right] q_w \cong \Omega^2\frac{2}{\pi}Rb\left(m + \frac{1}{2}\rho c C_L R\right) \tag{9}$$

The relative displacement at mid span is then

$$\frac{q_w}{R} \cong \Omega^2 \frac{\frac{4}{\pi}\left(1 + \frac{1}{2}\frac{\rho c C_L R}{m}\right)}{\pi^4 \frac{EJ}{mb^4} - \Omega^2\left(1 + \frac{\rho c C_L R}{m}\right)} \tag{10}$$

This equation applies to a simply supported blade. A clamped-clamped blade configuration is also considered. In this case, the first bending modal form is,

$$w(x,t) \approx \frac{1 + \cos\left(\frac{2\pi}{b}x\right)}{2} q_w(t) \tag{11}$$

and the same virtual work principle and derivations are followed. The deformation equation thus obtained for the clamped-clamped blade is,

$$\frac{q_w}{R} \cong \Omega^2 \frac{\frac{4}{3}\left(1 + \frac{1}{2}\frac{\rho c C_L R}{m}\right)}{\frac{16\pi^4}{3}\frac{EJ}{mb^4} - \Omega^2\left(1 + \frac{\rho c C_L R}{m}\right)} \tag{12}$$

which indicates by inspection that the influence of stiffness on limiting radial expansion will be roughly 5 times greater than in Eq. (10). It should however be noted that this does not translate directly into radial displacements because aerodynamic forces also contribute to radius changes.

The relative importance of the centrifugal and aerodynamic contributions to the stiffness and to the load is determined by the ratio

$$\tilde{\gamma} = \frac{\rho c R}{m} \tag{13}$$

This parameter plays the role that the Lock number[e] plays in helicopter aeromechanics: it is the ratio between the aerodynamic and the inertia loads. A gross approximation of the structural mass is $m = 2\rho_s ch$ where h is the thickness of the structural part of the blade, also known as the skin in conventional aeronautical structures, and ρ_s is the density of the structural material. The contribution of any filling material such as foam or honeycomb

---

[e] The Lock number [23] is defined as $\gamma = \rho C_{L/\alpha} c R^4 / I_\beta$ where $I_\beta \approx mR^3/3$ is the inertia moment of the helicopter rotor blade about the flap hinge.

could be added for a more precise estimation. As a consequence,

$$\tilde{\gamma} \approx \frac{\rho}{\rho_s} \frac{R}{2h} \tag{14}$$

The ratio ρ/ρ_s is of the order of 10^{-3}, whereas the ratio R/h is definitely greater than 1, and could be of the order of 10^3. As a consequence, the two contributions could be comparable, although $\tilde{\gamma} < 1$ is probably more likely. One should note that C_L may vary between $\pm C_{L_{\max}}$ within a revolution.

It is worth noting that all contributions to the external load, including those proportional to the configuration q_w, are proportional to Ω^2. As such, the deformation grows faster than quadratically, reaching a vertical asymptote at the divergence angular velocity Ω_D, which is for this simply supported beam

$$\Omega_D = \pi^2 \sqrt{\frac{EJ}{mb^4}} \frac{1}{\sqrt{1 + \tilde{\gamma}C_L}} \tag{15}$$

As expected, in the absence of aerodynamic forces Ω_D corresponds to the first natural frequency of the simply supported blade.

The aerodynamic forces, considering the bending of the blade, are

$$F_a = \frac{1}{2}\rho\Omega^2 cC_F \int_{-b/2}^{b/2} r^2 \, \mathrm{d}x = \frac{1}{2}\rho\,(\Omega R)^2\, bcC_F \left[1 + \frac{4}{\pi}\frac{q_w}{R} + \frac{1}{2}\left(\frac{q_w}{R}\right)^2\right] \tag{16}$$

where $r = R + \cos\left(\frac{\pi}{b}x\right)q_w$, as derived from Eq. (6), and C_F is the radial aerodynamic force coefficient resulting from the projections of the lift and drag coefficients. The increase in aerodynamic forces caused by the bending of the blade is thus

$$\frac{\Delta F_a}{F_{a_{\mathrm{ref}}}} = \frac{F_{a,\mathrm{flex}} - F_{a,\mathrm{rigid}}}{F_{a_{\mathrm{rigid}}}} = \Delta C_T = \frac{4}{\pi}\frac{q_w}{R} + \frac{1}{2}\left(\frac{q_w}{R}\right)^2 \tag{17}$$

which is quadratic in q_w.

The power required to counteract the aerodynamic forces, calling $F_\parallel$ the tangential component of the aerodynamic forces themselves, and $C_\parallel$ the related coefficient, is

$$\Pi_a = \frac{1}{2}\rho\Omega^3 cC_\parallel \int_{-b/2}^{b/2} r^3 \, \mathrm{d}x = \frac{1}{2}\rho\,(\Omega R)^3\, bcC_\parallel \left[1 + \frac{6}{\pi}\frac{q_w}{R} + \frac{3}{2}\left(\frac{q_w}{R}\right)^2 + \frac{4}{3\pi}\left(\frac{q_w}{R}\right)^3\right] \tag{18}$$

The increase in aerodynamic power caused by the bending of the blade is thus

$$\frac{\Delta\Pi_a}{\Pi_{a_{\mathrm{ref}}}} = \frac{\Pi_{a_{\mathrm{flex}}} - \Pi_{a_{\mathrm{rigid}}}}{\Pi_{a_{\mathrm{rigid}}}} = \Delta C_P = \frac{6}{\pi}\frac{q_w}{R} + \frac{3}{2}\left(\frac{q_w}{R}\right)^2 + \frac{4}{3\pi}\left(\frac{q_w}{R}\right)^3 \tag{19}$$

For example, for a mid span normalized deflection $q_w/R = 0.4$ one obtains $\Delta F_a/F_{a_{\mathrm{ref}}} \approx$ 0.6, and $\Delta \Pi_a/\Pi_{a_{\mathrm{ref}}} \approx 1$. This deflection amplitude, corresponding to 40% of the radius, occurs when $\Omega/\omega_1 \approx 0.5$. Limiting the analysis to the linear terms of ΔC_T and ΔC_P and considering $E_r = C_T/C_P$ as a measure of the efficiency, the sensitivity to the normalized deflection is

$$\frac{\partial E_r}{\partial(q_w/R)} = \frac{1}{C_P}\left(\frac{\partial C_T}{\partial(q_w/R)} - E_r\frac{\partial C_P}{\partial(q_w/R)}\right) \tag{20}$$

which is greater than zero only when

$$\frac{\partial C_T}{\partial(q_w/R)} > E_r\frac{\partial C_P}{\partial(q_w/R)} \tag{21}$$

i.e. for $E_r < 2/3$. Therefore, the bending of the blade causes a reduction of the aerodynamic efficiency except at very low values of efficiency.

The analysis has been extended to the case of coupled bending-torsion. This coupling occurs when either the elastic axis or the center of mass is offset from the aerodynamic center, or both. The aerodynamic center is chosen as the feathering axis. Placing the shear center and the center of mass at the aerodynamic center decouples the two problems. As for the general case of fully coupled problems, only a numerical analysis based on the multibody solver will be presented.

III.   Multibody aeroelastic analysis

A.   Actual vs. ideal rotor

The multibody model of cycloidal rotors developed for this paper differs slightly from the real rotor. The real rotor has the geometry presented in Fig. 2 where the pitch of each blade is controlled cyclically by a pitch rod mechanism. As such, the blades are connected to the central drum by the pitch rods at a location close to the rotation axis of the drum itself. The attachment location on the drum remains fixed in space while the drum rotates, and thus forces the blade pitch angles to harmonically change while going around their rotation axis. Moving the point of attachment allows vectoring the thrust produced by the rotor. This creates a nearly sinusoidal 1/rev pitch control. The cycloidal under study is sized to match the Yun *et al.* [22] experimental prototype of Table 1.

Flexibility causes the rotor radius to vary along the span of the blade. When modeling in two-dimensions, there exists an optimal radius which gives the best efficiency. Thus, flexibility impedes having the optimal radius on the whole span of the blade. Blade deformations were also shown to be potentially important [12]. Thus, to avoid a reduced efficiency, a

Table 1. **Description of the experimental data.**

Author	Radius (m)	Span (m)	Chord (m)	N. of foils	3D control
Yun *et al.* [22]	0.4	0.8	0.15	6	Arms at edges
IAT21 [24]	0.6	1.2	0.3	6	Disks at edges
McNabb [25]	0.610	1.22	0.301	6	Disk at midspan

clamped beam approach is used in this study in order to limit blade bending. In practice, such a clamping could be implemented as a combination of two bearings aligned with the blade pitching axis at each blade edge so as to prevent local bending. The rotor blades would thus be attached to bearings at the end of the pivot rods shown in Fig. 2.

B. Model implementation

The multibody model uses finite-volume nonlinear beam elements [26], with aerodynamics based on blade element and lookup-table static airfoil properties. It also uses simple inflow models based on Momentum Theory that have been specifically developed for the analysis of cycloidal rotors [12]. Its geometry is similar to the real rotor described just above with the following difference: the blade pitching angle is set by a function and thus no pitch link is modeled. The pitching motion is applied to the edges of the blades at their pitch axis, which is where the pivot rods would be attached. The deformation of the blades creates a change in the radial distance between airfoil and rotor center. Changes in the angle of attack and twist of the blade are also taken into account by the model. The pitching schedule is thus modeled as ideal according to the following equation,

$$\theta = \theta_0 + \sum_{n=1}^{2} (\theta_{cn} \cos n\psi + \theta_{sn} \sin n\psi) \tag{22}$$

where ψ is the angular position of the main drum and θ_i are constants chosen according to the desired pitch magnitude. It has been shown [27] that this pitching function differs minimally with the real mechanism used to control a cycloidal rotor.

The purpose of this model is to study the influence of the blade structural properties on the moment that will be sustained by the blade supporting rods. This moment corresponds to M_y in Fig. 6 where the pitch rod is shown only for reference because in the multibody model, the pitching motion is imposed as an additional rotation between the drum and the blade multibody nodes. The pitch rod is a possible control mechanism but is of no interest in this part of the analysis because various other types of pitch control could be used. One such pitch control strategy would be to use an electric drive. Regardless of the control strategy, for clamped blades, the moments M_y will be sustained by the pivot rods, because they restrain

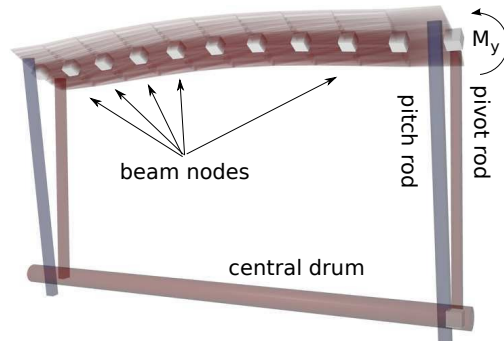the blades from bending at the edges.

Figure 6. Multibody model configuration.

The schematic representation of one blade of the flexible multibody model is shown in Fig. 6. The small cubes represent the nodes of the model. Those of the blade are connected in groups of three using the MBDyn beam finite volume method [26] to create a flexible blade. The isolated bottom node is the main drum and is imposed a constant rotation velocity. It is attached to the nodes at the edges of each blade by a combination of two joints. The first is a joint which imposes the pitch rotation about the local blade pitching axis. The second is a revolute joint and prevents any rotation in roll or yaw of the blades, which are axes 2 and 3, respectively, on Fig. 7(c). The revolute joint also fixes the relative translation between the drum and blade nodes. The actual links between the main drum and the blade edges thus have the only constraint, imposed by the multibody model, of being rigid. Finally, a series of flexible beam elements is used to attach together the nodes of each blade.

For the simplicity of the analysis and the possibility to model various flexibility scenarios, a simple blade structure geometry is assumed. It is shown in Fig. 7. The structural data of the aluminum 6061-T6 used for the structure of this aeroelastic model is reported in Table 2. The stiffness properties are calculated from the wing geometry which is drawn in Fig. 7(c).

Table 2. Aeroelastic model structural properties.

Young's modulus E_{al}	70.0	GPa
shear modulus G_{al}	26.0	GPa
density ρ_{al}	2700.0	kg/m^3
yield strength σ_y	241.0	MPa
ultimate tensile strength	300.0	Mpa

From this geometry, the parameters necessary for the multibody simulation are reported in Table 3 which also gives the baseline model dimensions. The other rotor dimensions are taken from Yun *et al.* [22] and were reported in Table 1. It is assumed that the wall thickness t_f remains small relative to the airfoil height. The variable M_{yb} is the moment

(a) Structure used to represent the blade.

(b) Dimensions of the outer edges.

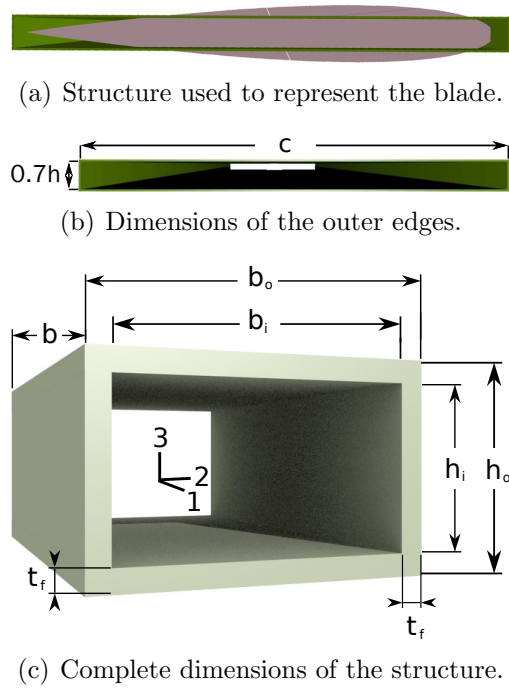(c) Complete dimensions of the structure.

Figure 7. Blade modeling as an extruded aluminum rectangle.

which is aimed to be sustained by the arm at an angular velocity of 110 rad/s (1050 rpm). It serves to calculate the corresponding thickness t_f. An iteration procedure found the t_f which brings, at that angular velocity, the bending moment sustained by the bearing joint to $M_y = 190$ Nm. This value is acceptably close to the target value of $M_{yb} = 200$ Nm. It was also ensured that this thickness maintains the shear stress well below the yield stress at every angular velocity considered. The outer height h_o of the rectangular structure is selected as 70% of the actual airfoil height and its outer width b_o is equal to the chord. The purpose of the present model is to examine the influence of aeroelastic aspects on performances. The results presented should thus be considered in terms of perturbations with respect to nominal, rigid blades, rather than in terms of absolute values.

C.   Model validation

The results of the rigid version of the multibody analysis were compared with the experimental aerodynamic data taken from three different sources for which the geometric parameters were given in Table 1.   The multibody model was calibrated for optimal κ and ζ which are the empirical correction coefficient and the aerodynamic drag coefficient corrector, respectively. The resulting plots are shown in Fig. 8, which compares with the Yun *et al.* [22] experimental data of their baseline model at various pitching function magnitudes, the Mc-Nabb [25] experimental data of a 6 blade model at 25° magnitude pitch function, and the IAT21 [24] experimental data of the D-DALUS L3 model at 37.5° magnitude pitch function.

Table 3. Aeroelastic model structural properties.

|				
Area	A_1	$b_o h_o - b_i h_i$	2.82	cm^2
Area	A_2	$b(h_o - h_i)$	1.41	cm^2
Area	A_3	$b(b_o - b_i)$	1.41	cm^2
Safety factor	S_F	-	2.	
Targeted bending moment	M_{yb}	-	200.	Nm
Wall thickness	t_f	$\frac{S_F M_{yb}}{h_o c^2 \sigma_y}$	0.878	mm
Beam outer length	b_o	c	15.0	cm
Beam inner length	b_i	$b_o - 2t_f$	14.8	cm
Beam outer height	h_o	$0.7 \times c \times 0.12$	1.26	cm
Beam inner height	h_i	$h_o - 2t_f$	1.08	cm
Second moment of area	I_{22}	$\frac{1}{12}(b_o h_o^3 - b_i h_i^3)$	0.925	cm^4
Second moment of area	I_{33}	$\frac{1}{12}(h_o b_o^3 - h_i b_i^3)$	60.0	cm^4
Torsion factor	K_{11} [28]	$\frac{2t_F b_i^2 h_i^2}{(b_o + h_o - 2t_f)}$	2.82	cm^4
Blade mass	M	$2\rho_{al} b t_f (b_o + h_i)$	610.	g
Axial stiffness	EA	$E_{al} A_1$	19.8	MN
Shear stiffness	GA_y	$G_{al} A_2$	36.5	MN
Shear stiffness	GA_z	$G_{al} A_3$	36.5	MN
Torsional stiffness	GK	$G_{al} K_{11}$	0.734	kNm^2
Bending stiffness	EJ_y	$E_{al} I_{22}$	0.648	kNm^2
Bending stiffness	EJ_z	$E_{al} I_{33}$	42.0	kNm^2

The multiplication factor ζ, was used on the standard aerodynamic drag coefficient tables of the NACA-0012 airfoil. The results in Figs. 8(c) and 8(d) were computed using a large value for the blade drag coefficient multiplier ζ. That value was obtained by minimizing the multibody model error. This was expected because McNabb [25] also greatly increased the blade drag coefficient when modeling the cycloidal rotor results and mentioned high drag on the blades used experimentally.
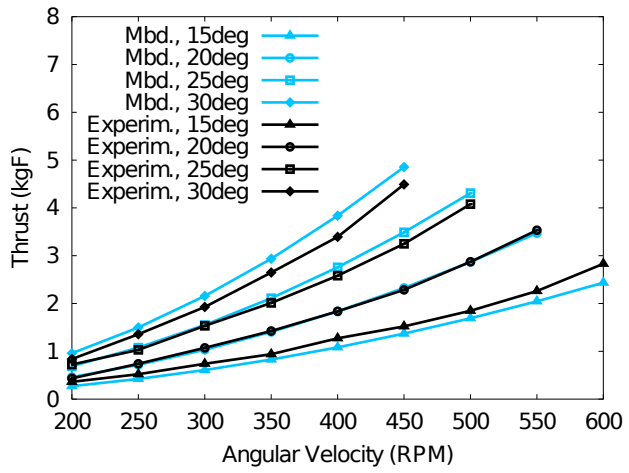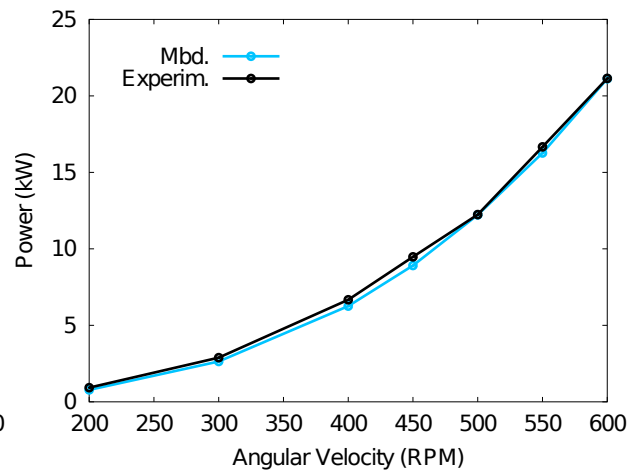
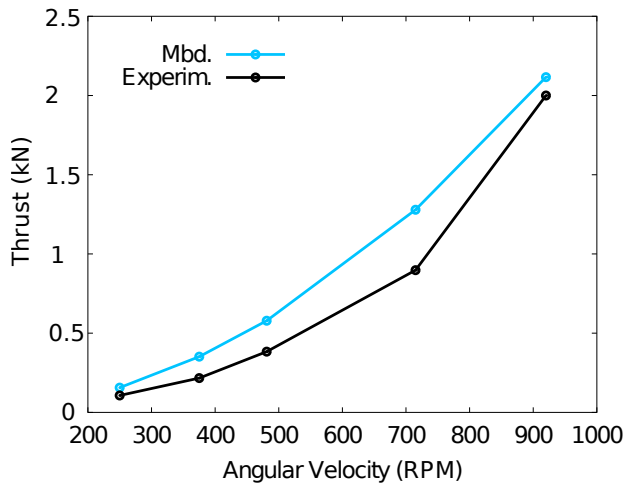(a) Yun *et al.* T vs. Ω. $\kappa = 1.4804$ and $\zeta = 3.63$
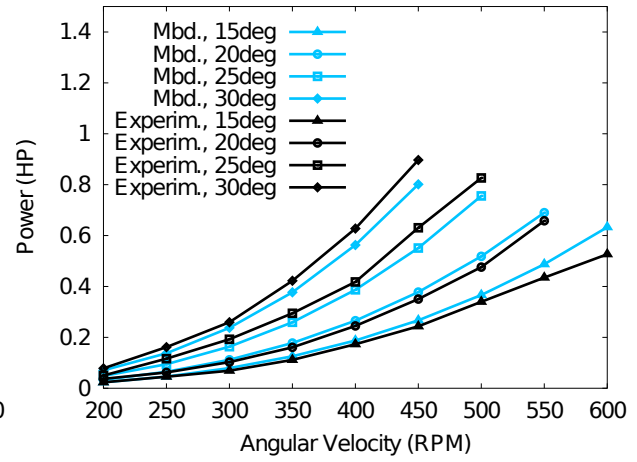
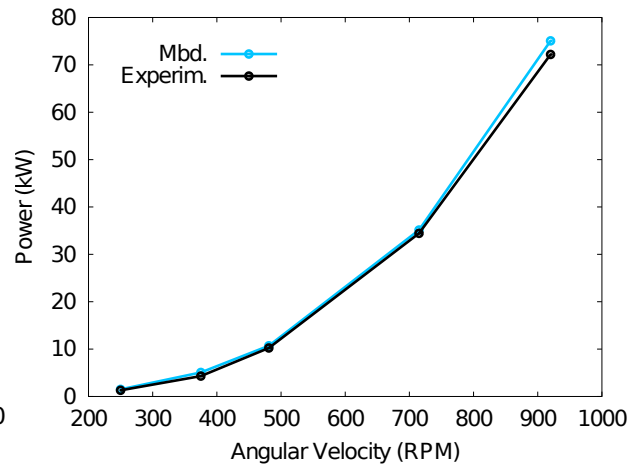(b) Yun *et al.* P vs. Ω. $\kappa = 1.4804$ and $\zeta = 3.63$
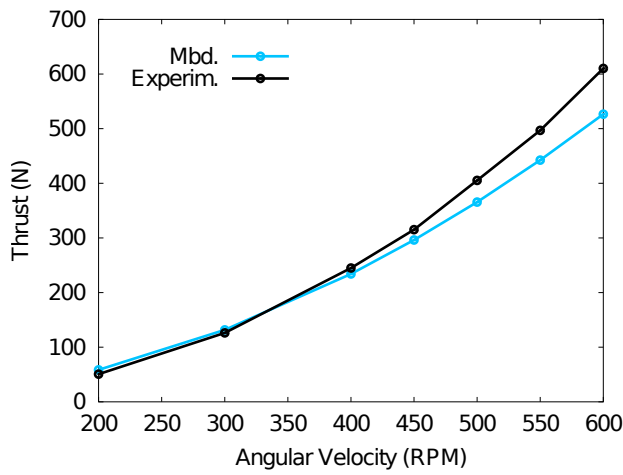
(c) McNabb T vs. Ω. $\kappa = 1.0785$ and $\zeta = 12.0$.

(d) McNabb P vs. Ω. $\kappa = 1.0785$ and $\zeta = 12.0$.

(e) IAT21 T vs. Ω. $\kappa = 1.2640$ and $\zeta = 1.00$.

(f) IAT21 P vs. Ω. $\kappa = 1.2640$ and $\zeta = 1.00$.

Figure 8. **Comparison with the Yun *et al.* [22], McNabb [25], and IAT21 [24] experimental data.**

D.   Solidity analysis

The validation assessed that the rigid multibody model is suitable for use in this study. This section covers the influence of rotor solidity using the rigid blade version of the multibody model. For every further simulation reported in this paper, the geometric parameters of Yun *et al.* [22] are used. The rotor was thus configured to produce forward thrust and tests are reported over the remainder of this article. Four configurations were initially studied to measure the impact of the number of blades on rotor performance. They are cycloidal rotors with 2, 3, 4, and 6 blades of the type shown in Fig. 9, where the dimensions shown are not indicative of the tested models.
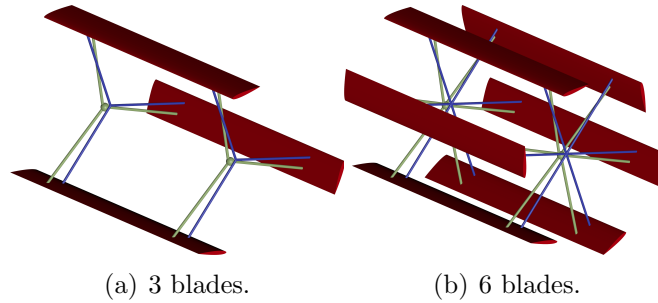

(a) 3 blades.   (b) 6 blades.

Figure 9. Multibody models for different solidity configurations.

Figure 10 shows the thrust and power coefficients for rigid blade configurations of increasing solidity, with 2, 3, 4, and 6 blades, at 40° cyclic pitch angle maximum magnitude. Such a pitch angle magnitude, in conjunction with the downwash produced by the inflow, sets the operating condition of the airfoils in proximity of stall. The thrust and power coefficients used in the figures were previously defined by Eqs (3) and (4). The variable σ represents the solidity, which is the ratio of the total area covered by the blades to the lateral cylindrical area of the drum,

$$\sigma = \frac{cbN}{2\pi Rb} = \frac{cN}{2\pi R} \tag{23}$$

while the Power Loading (PL) and Disk Loading (DL) are defined respectively as,

$$PL = \frac{T}{P} \tag{24}$$

and

$$DL = \frac{T}{2Rb} \tag{25}$$

Figure 10 shows that the thrust coefficient, at constant pitch angle, is relatively insensitive to the rotational speed up to roughly 1200 rpm. Different values are obtained for different number of blades. The figure suggests that the 6 blade configuration gives the largest C_T/σ
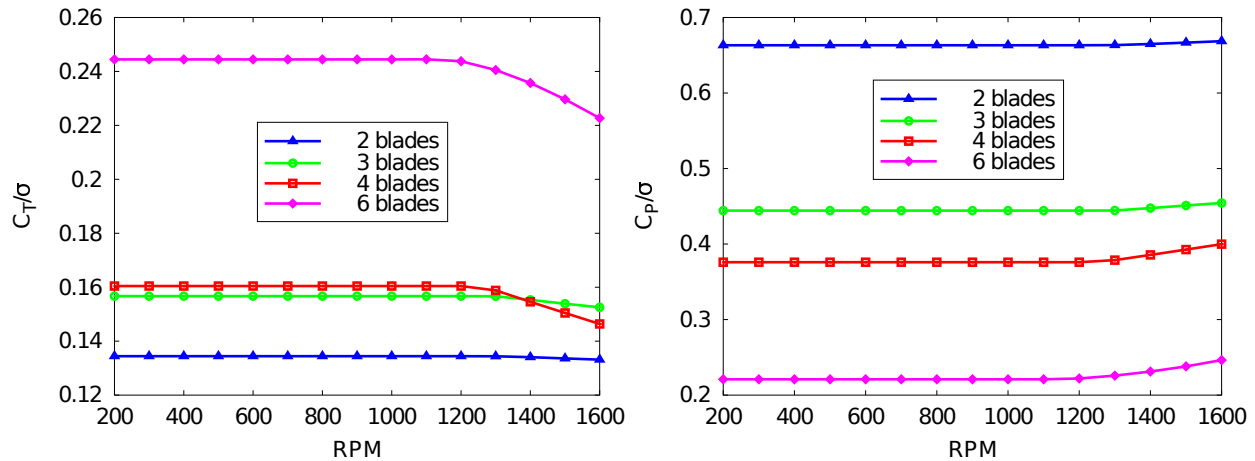
Figure 10. Thrust and power coefficients at 40° cyclic pitch with rigid blades.

and lowest C_P/σ. It is also found that the maximum pitch angle has a considerable effect on the coefficients, as seen when comparing Figs 10 and 13. This is explained by the blades behavior of producing inconsistent lift at high pitch angles due to stall.
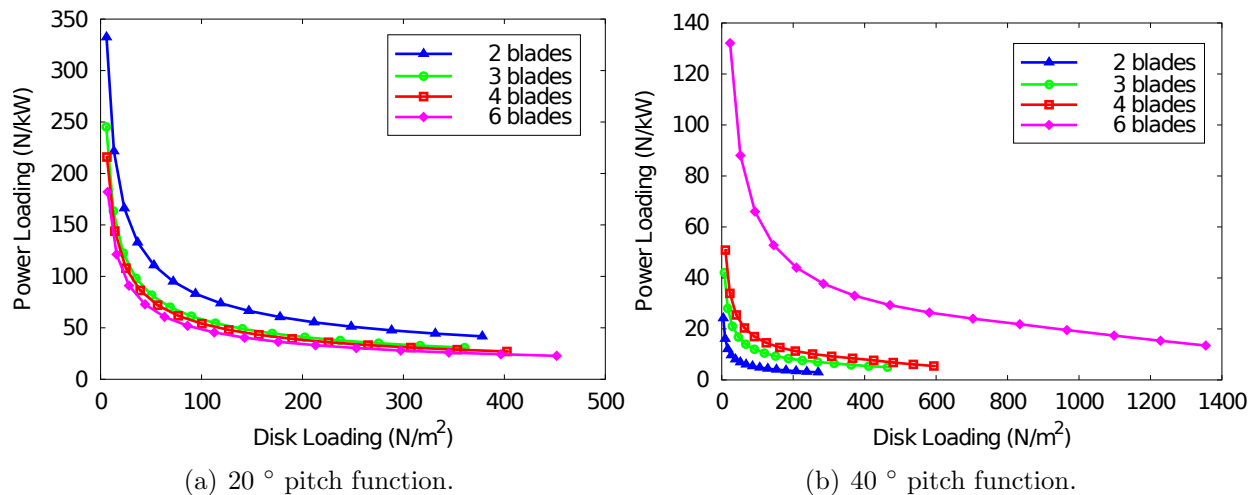

(a) 20 ° pitch function.

(b) 40 ° pitch function.

Figure 11. Influence of solidity using the rigid model.

Figure 11(a) reproduces the same trend as the one obtained by Xisto *et al.* [24] from an experimentally validated CFD model. The shapes of the curves are also consistent with their output which showed higher PL at low DL and lower PL at high DL. The tendency of the trend to revert is also observed both by Xisto *et al.* [24] and the results of Fig. 11(b). Surprisingly, the numerical values are similar for the curves of Fig. 11 and those of Xisto *et al.* [24], even though they used a different rotor geometry. Some differences may also be explained because at large N the value of solidity grows substantially and this implies significant flow blockage. For example, the solidity of the current configuration with 6 blades

is $\sigma = 0.36$. This value is much higher than for an helicopter. The blockage effect cannot be captured by a blade element model but is however considered by the empirical inflow correction coefficient, κ, which is similar to the ones used by [22] and [23].

Low solidity is preferable for practical applications of cycloidal rotors, as discussed in [20]. However, the 6 blade configuration is advantageous in terms of PL vs. DL at 20° and in terms of C_T/σ at 40° pitch. This configuration is also the most common in the literature, for the Reynolds number range considered here. Therefore, the remainder of the analysis focuses on a 6 blade configuration.

E.   Influence of stiffness

The flexibility of the blades in the multibody model is activated and the study is thus carried forward with the 6 blade model having the dimensions of Yun *et al.* [22] reported in Table 1. Figure 12 compares the corresponding PL vs. DL at two pitch function magnitudes. It once again highlights the important impact of high pitch angles. Figure 13 shows the influence of material rigidity on the thrust and power outputs of the rotor. More flexibility increases both thrust and power values.
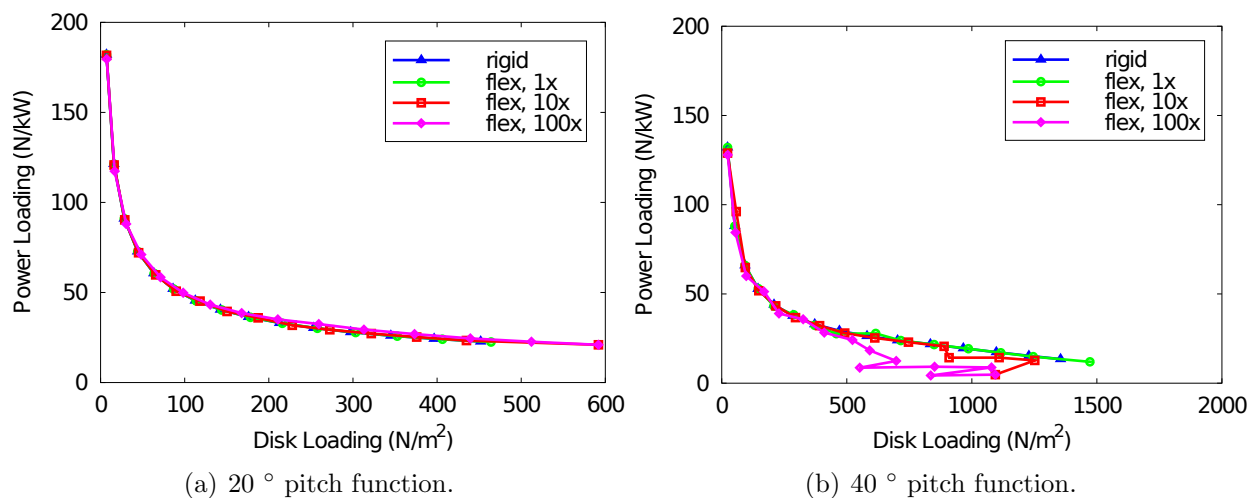

(a) 20 ° pitch function.   (b) 40 ° pitch function.

Figure 12.   Comparison of rigid and flexible blades.

At 20° cyclic pitch the angle of attack is smaller, and far away from stall. As a consequence, a much smoother behavior is observed in the curves of Fig. 12(a) than of Fig. 12(b). The previous considerations for the divergence angular velocity do however still hold. Seeing that the rigid and the flexible curves nearly overlap in Fig. 12(a), the increase in thrust and power related to the elastic deformation of the blades observed in Fig. 13 has a negligible impact on the PL vs. DL curve.

The influence on the bending moment resulting from variations in the structural properties of the blades by two methods is examined. The first one changes the material properties
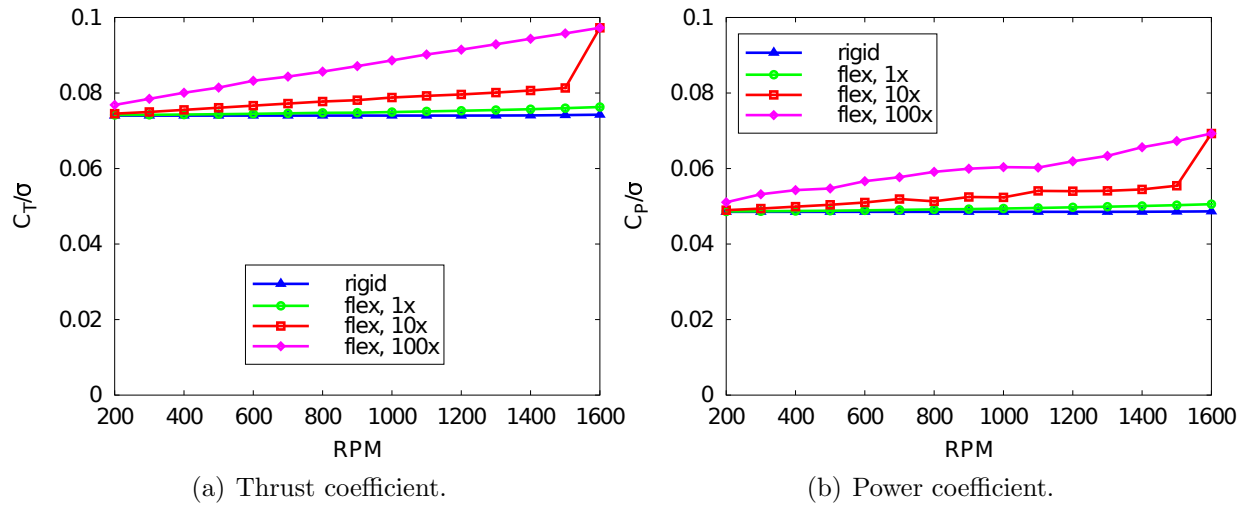
(a) Thrust coefficient.

(b) Power coefficient.

Figure 13. Comparison of rigid and flexible blades at 20° cyclic pitch.

by multiplying the Young's modulus and the shear modulus by a factor. This is the method used in Figs 12 and 13 where the moduli are divided by 10 and 100 for the 10x, and 100x flexibility cases, respectively. The same approach is used for Fig. 14(a), where the moduli are multiplied by 1/10 and 10, for the 10/1 and 1/10 flexibility cases, respectively. The second method changes the thickness of the structural rectangular box representing the blade, which is referred to as the skin in this article. The effect is shown in Fig. 14(b). One should note that changing this thickness also changes the blade weight and consequently the centrifugal forces.
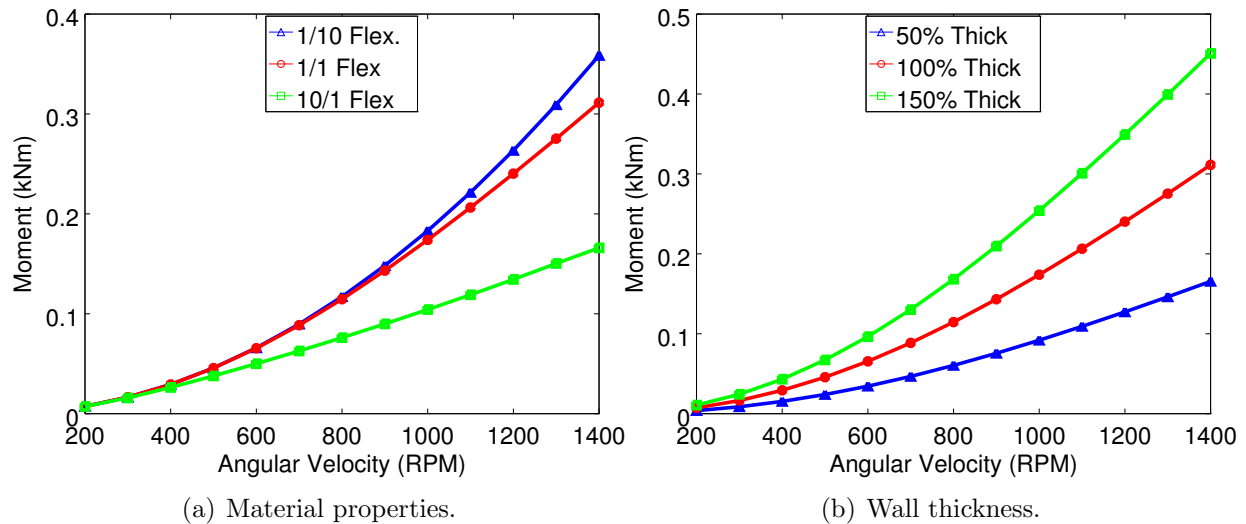

(a) Material properties.

(b) Wall thickness.

Figure 14. Effect of structural modifications on the bending moment sustained by the blades.

The analysis suggests that aeroelasticity has negligible effects when using the initial blade properties. The effects become considerable for the blade with a 100 times higher

flexibility. It is calculated that, using Eq.(15), centrifugal divergence occurs slightly above 2000 rpm. At higher angular velocities, the multibody analysis does not quickly converge to a steady operating condition. Instead, large deflections and oscillations occur, thus leading to instantaneous angles of attack well beyond static stall and erratic behavior. For this reason, data points above 1400 rpm are for the most part not reported. In any case, the deflections at such angular velocity values are already quite pronounced.

The results revealed that the blade maximum and minimum radius deformations remain the same for each of the 6 rotor blades. The model allowed to observe the influences on radii, generated thrust, and required power which are shown in Figs 15 and 16. From these, it can be said that increasing the flexibility of the blades by decreasing the rigidity of the material, as shown in Fig. 14(a), has a strong influence on the moment sustained by the pivot rod. A stiffer blade requires a stronger pivot arm. This same behavior is also observed in Fig. 14(b), where the thicker blade walls cause an increase in the sustained moment. As expected, the radius of the blade at midspan increases with flexibility. Figure 15(a) shows the maximum radius the blade will attain over a rotor revolution. The rate of this radius increase curve varies with the angular velocity and the flexibility of the blade. This is due to the complex relationship between blade bending and elongation. Interestingly, changing the thickness of the airfoil structure has little influence of the maximum blade radius, as seen in Fig. 15(b). Effectively, the benefits of the stronger thicker blade walls are canceled out by the increase in centrifugal force caused by the higher blade weight. Similar radius behaviors are observed for the minimum blade radius over a cycle, as shown in Figs. 16(a) and 16(b). These figures show the minimum radius the blade will have at midspan over one rotor revolution, and when compared with Figs 15(a) and 15(b) they reveal that the main contributor of blade radius increase is constant. In Fig. 16(c), the influence on the resulting thrust is rather small, but using a more malleable material does slightly increase the thrust produced. The accompanying result is that power also increases for a more malleable material, as shown in Fig. 16(e). The thrust and power changes directly result from the changes in blade radius because the changes in angles of attack are infinitesimal due to the strong resistance to torsion of the rectangular blade structure.

As a means of comparison, the analytical model of Section II has been used with the same geometric and structural parameters which were defined for the multibody model. Thus, using the formulation for simply supported blades of Eq. (10), Figs. 15(c) and 15(d) are obtained. The strong influence of the divergence angular velocity also appears in Fig. 15(c) as the asymptotic line. As expected, larger deformations occur at higher flexibility values. As for wall thickness, the influence is not so intuitive because the wall thickness influences both mass and rigidity.

To obtain a better basis for comparison, the clamped-clamped wing configuration solution

of Eq. (12) is relied upon. Figures 15(e) and 15(f) are obtained and correlate well with the multibody model results both in tendency and magnitude. They also confirms the intuitive fact that a simply supported blade will deform significantly more than a clamped one.

Finally, to obtain the analytical solutions of Fig. 15, it is assumed that the greater rotor radius occurs when the coefficient of lift C_L is at its maximum. This occurs for the greatest angle of attack encountered. It was assumed to equal the magnitude of the pitch angle function θ_{c1}, the only non null input to Eq. (22). This assumption is not exactly true because, when producing forward thrust, the blades will be subjected to an inflow which reduces the angle of attack at the position of maximum blade pitching angle. A further analysis may be conducted by using the equations presented in a related work [29] where the equation of the angle of attack is given. Other explanations for the differences between the radius increase, measured by the two models, are that the multibody model uses tabular drag and lift data; computes the exact lift coefficient; calculates the resulting inflow; and, accounts for the flexibility-induced delay in the response.

F. Wind gusts

The EASA CS-25 recommendations [30] are used to investigate the effect of a range of wind gusts on the behavior of the flexible-blades cycloidal rotor. In particular, the effects on the responses in power consumption, in thrust generation, and in the blade support moments are studied. Once again, the blades are in a clamped-clamped configuration. Care is also taken to cover the extreme cases. Although the CS-25 specifications apply to large airplanes, they were deemed appropriate to give a good sampling of gusts to which cycloidal rotors could be subjected.

The calculations are done on a rotor fixed in position and producing forward thrust in calm air. The gust parameters are adjusted as if the aerial vehicle were traveling at 10 m/s. In all cases reported, the gust onset is applied after the rotor reaches a stable regime. The gust function used is, as given by EASA [30],

$$U = \frac{U_{ds}}{2} \left[1 - \cos \frac{\pi s}{H} \right] \tag{26}$$

where

$$U_{ds} = U_{ref} F_g \left(\frac{H}{107} \right)^{1/6} \tag{27}$$

for which the variables are defined in the EASA recommendations.

The first observations come from the comparison of the response of the flexible airfoil rotor producing forward thrust in calm air with its response when subjected to a gust front. The front arrives at 10 m/s and has the maximum reference velocity $U_{ref} = 17.17$ m/s and
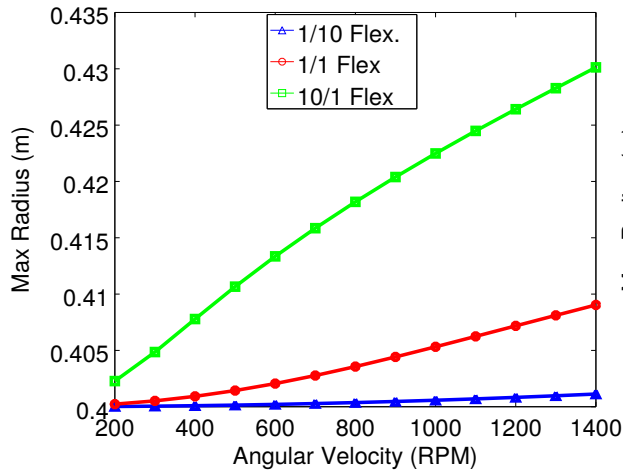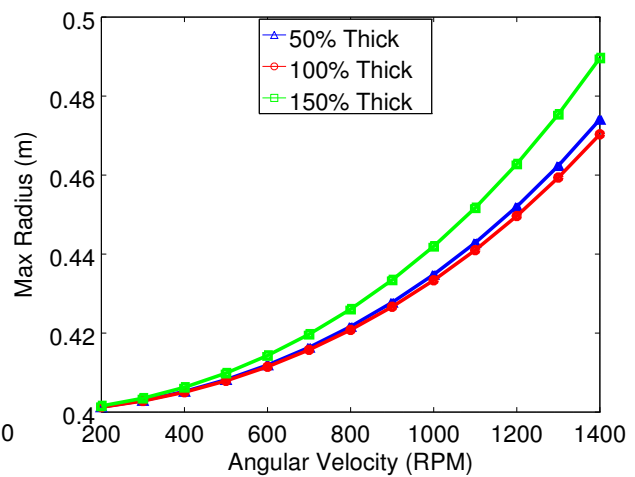
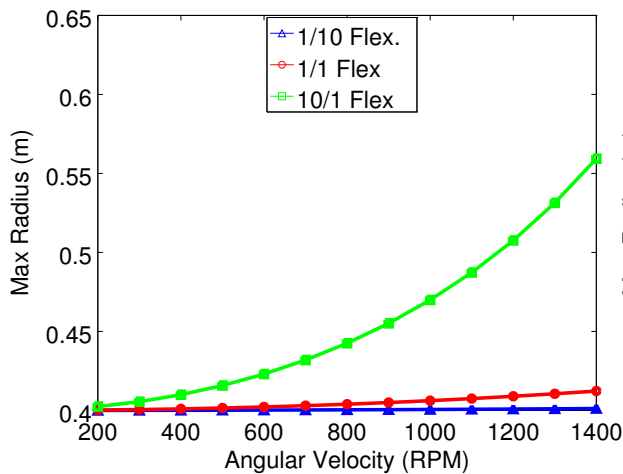(a) Material properties. Multibody. Clamped.
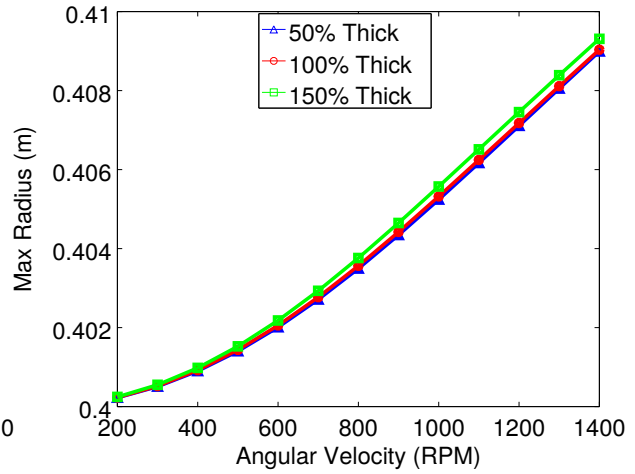
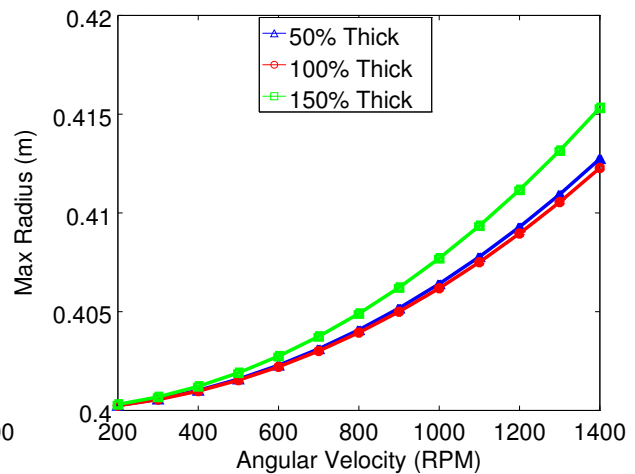(b) Wall thickness. Multibody. Clamped.
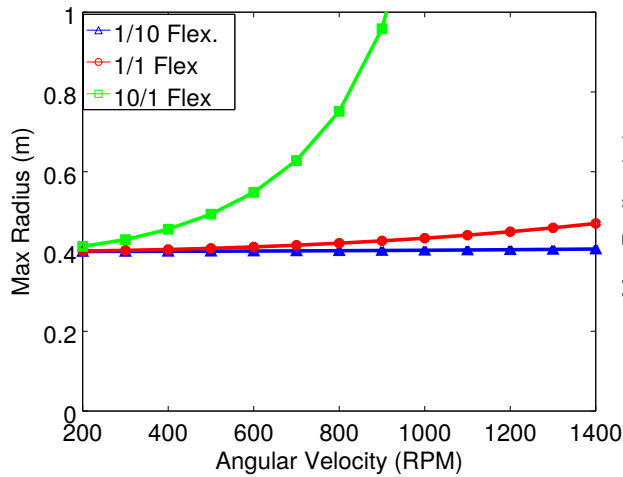
(c) Material properties. Analytic. Simply supported.

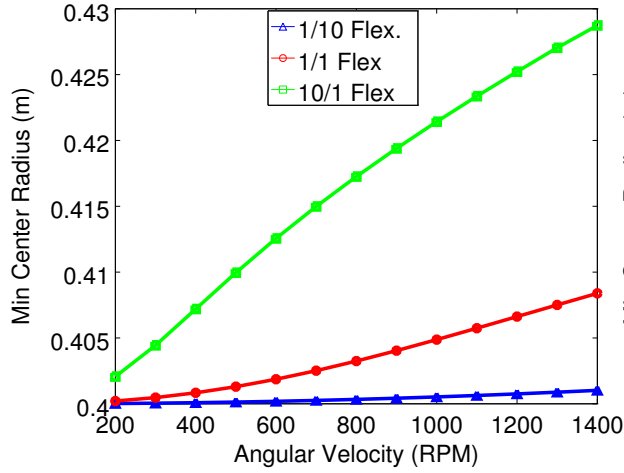(d) Wall thickness. Analytic. Simply supported.

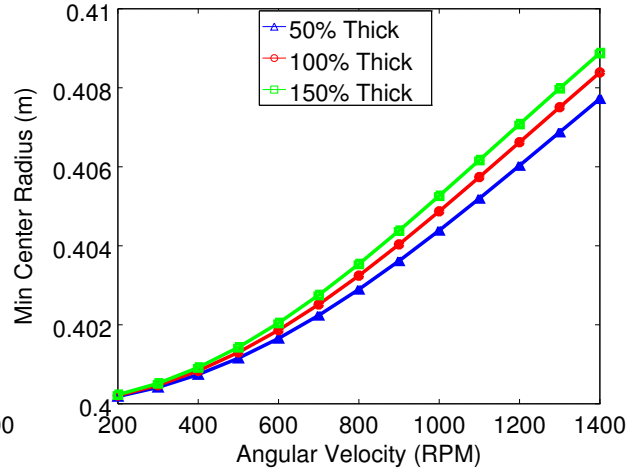(e) Material properties. Analytic. Clamped.

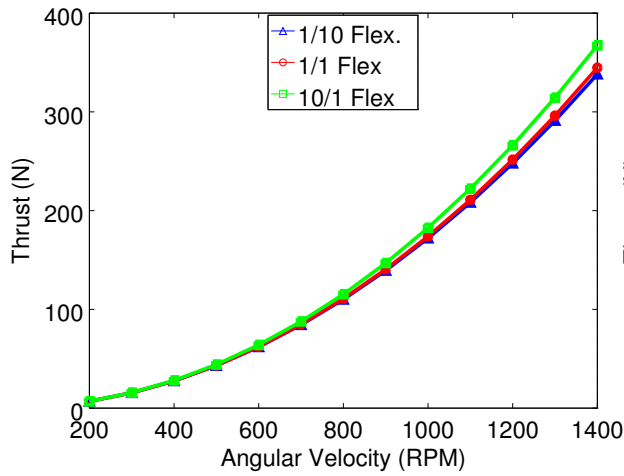(f) Wall thickness. Analytic. Clamped.

Figure 15. Effect of structural modifications calculated using the multibody model and the analytical solution.
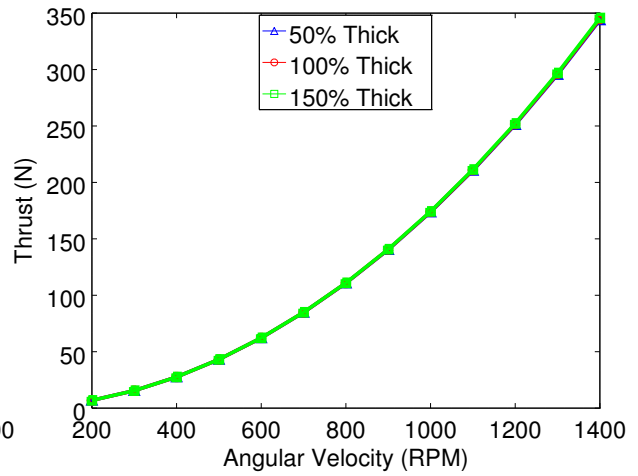
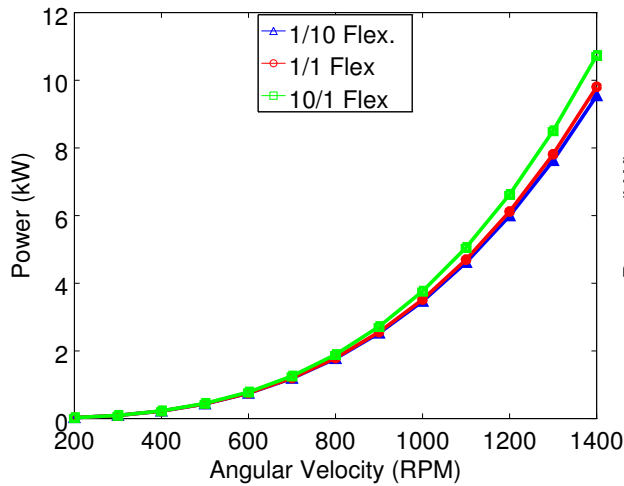(a) Effect of material properties.
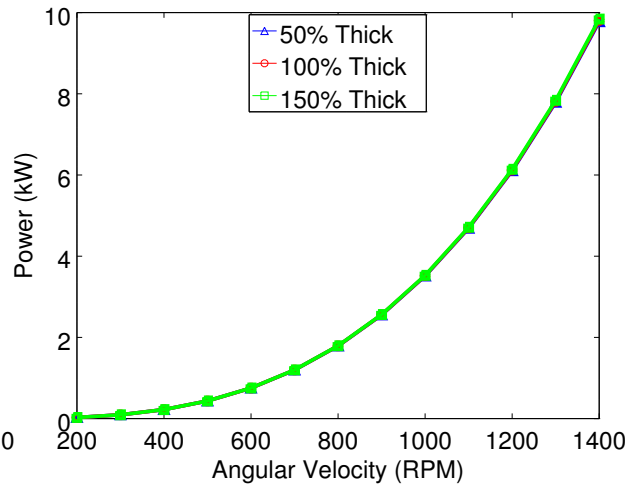
(b) Effect of wall thickness.

(c) Effect of material properties.

(d) Effect of wall thickness.

(e) Effect of material properties.

(f) Effect of wall thickness.

Figure 16. Effect of structural modifications.

minimum gradient $H = 9$ m, as specified by the EASA. This configuration is chosen as it gives the strongest gust impact. Figure 17 shows the impact felt by the rotor when crossing that gust. The differences shown correspond to the increase in percentage that the gust causes to the value considered. Care should be taken when interpreting the values at the very lowest rpms because it is possible that the gust does not cover the time required to perform a full revolution of the rotor. The rotor thrust and power shown correspond to the maximum values over the period starting at the onset of the gust and lasting 15% longer than the gust. The mean values are not presented because they are influenced by the number of revolutions the rotor will complete during the gust.

(a) Arm moment.　　　　(b) Blade shear stress.　　　　(c) Max. blade radius.

(d) Rotor power.　　　　(e) Rotor thrust.　　　　(f) Min. blade radius at center.
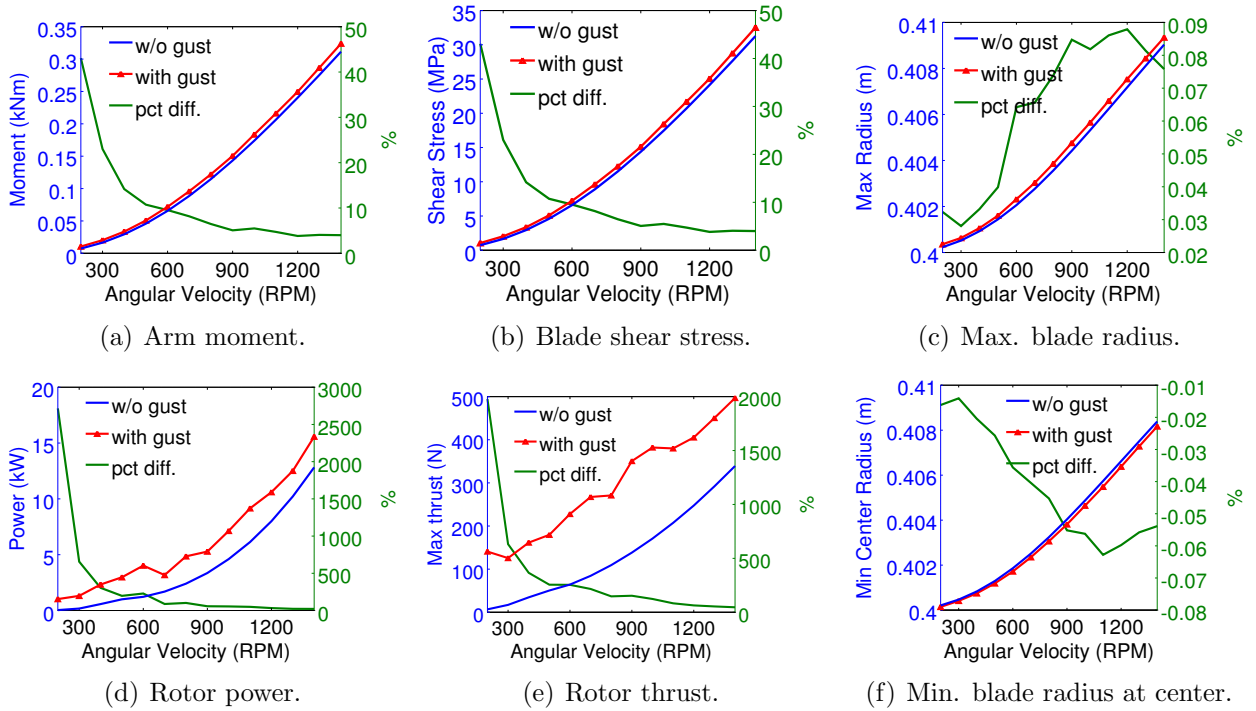
Figure 17. Effects of the strongest gust. Maximum values over the gust influence period are shown.

The gust is always applied after a steady condition is reached and at the same angular position of the rotor for every angular velocity considered. The initial time of the gust is thus,

$$t_i = \left\lceil \frac{\Omega}{4.8} \right\rceil \frac{2\pi}{\Omega} \tag{28}$$

where $\Omega/4.8$ is a function of the angular velocity Ω which approximates the number of revolutions required to reach stability. It is rounded up to give an integer and thus always yield the same rotor angle at the gust initial time. The integer is then multiplied by the time required to complete one rotor revolution, which is $2\pi/\Omega$.

As predicted, the effect of the gust is to increase the blade deformation and thus internal

shear stress and rotor arm moment. The minimal center radius of a blade also decreases. This is due to the fact that over a rotor revolution, the blade will be influenced by the gust on both its sides. On one side it helps and on the other side it counters the centrifugal forces. No dramatic increase in stress or moment are observed. Thus, minimal modifications to the blade geometry would allow to sustain the prescribed gusts. At low angular velocities the stress increases are small and thus not of structural interest. If it is assumed that an electric motor controller would maintain a constant angular velocity, the mean thrust increases when crossing the gust. This is at least the case when the gust wind direction is perpendicular to the undisturbed rotor thrust. The mean power variations depend on the angular velocity and this is likely due to the more sensitive relation between power and incoming wind. The shear stress is exactly proportional to the moment, as seen previously in Fig. 17.

The impact of the gust strength is shown in Fig. 18. The effects of gust gradients and reference velocities on the maximum thrust produced by the blades during the gust influence period, on the bending moment sustained by the blades, on the power required by the rotor, and on maximal and minimal blade radii at center span are shown. The figure shows gust strengths of positive and negative 17.07 m/s along with a 0 m/s, which is the absence of a gust. The plots of various gust gradients are shown for the maximum magnitude of 17.07 m/s. Figures 18(a) and 18(b) show the influence on the maximum thrust during the gust under various gust strengths and gradients. They show that the thrust increase is mostly caused by the push of the gust. They also show that a smaller gradient creates a more pronounced increase of thrust and that there is apparently an optimal angular velocity for this increase. The effect of various gust strengths and gradients are shown in Figs. 18(c) and 18(d), where a non-dimensional representation is used to better show the differences between the different strengths and gradients. The non-dimensional moment is defined as,

$$10^7 M_y (rpm)^{-1.78} \tag{29}$$

It is seen that the gust gradient and velocity influences on moment and shear stress are smaller, but larger in proportion, at low angular velocities. A smaller gradient and a higher velocity both increase the moment. A negative velocity however leaves the moment unchanged at high rpm. Figures 18(e) and 18(f) show the influence on the maximum power during the presence of the gust. A non-dimensional interpretation similar to the one for the moment is used. It is seen that the effect of the gust gradient on power is similar than for thrust. The influence of gusting wind velocity on power is different, and depends strongly on the direction of the wind. This is however only the case at high rpm, while the tendency establishes itself gradually between 300 rpm and 900 rpm. The proportion of the change in power is higher at low angular velocities. Finally, Fig. 18(g) to 18(j) shows the influences

of the gusts over a rotor revolution on the maximum and minimum blade radii at midspan. Again, the non-dimensional form of Eq. (29) is used to highlight the difference between the various gusts. The changes on radii remain minimal for every gust considered.

(a) Effect of gust gradient.

(b) Effect of gust reference velocity.

(c) Gust gradient.

(d) Gust ref. velocity.

(e) Gust gradient.

(f) Gust ref. velocity.

(g) Gust gradient.

(h) Gust ref. velocity.

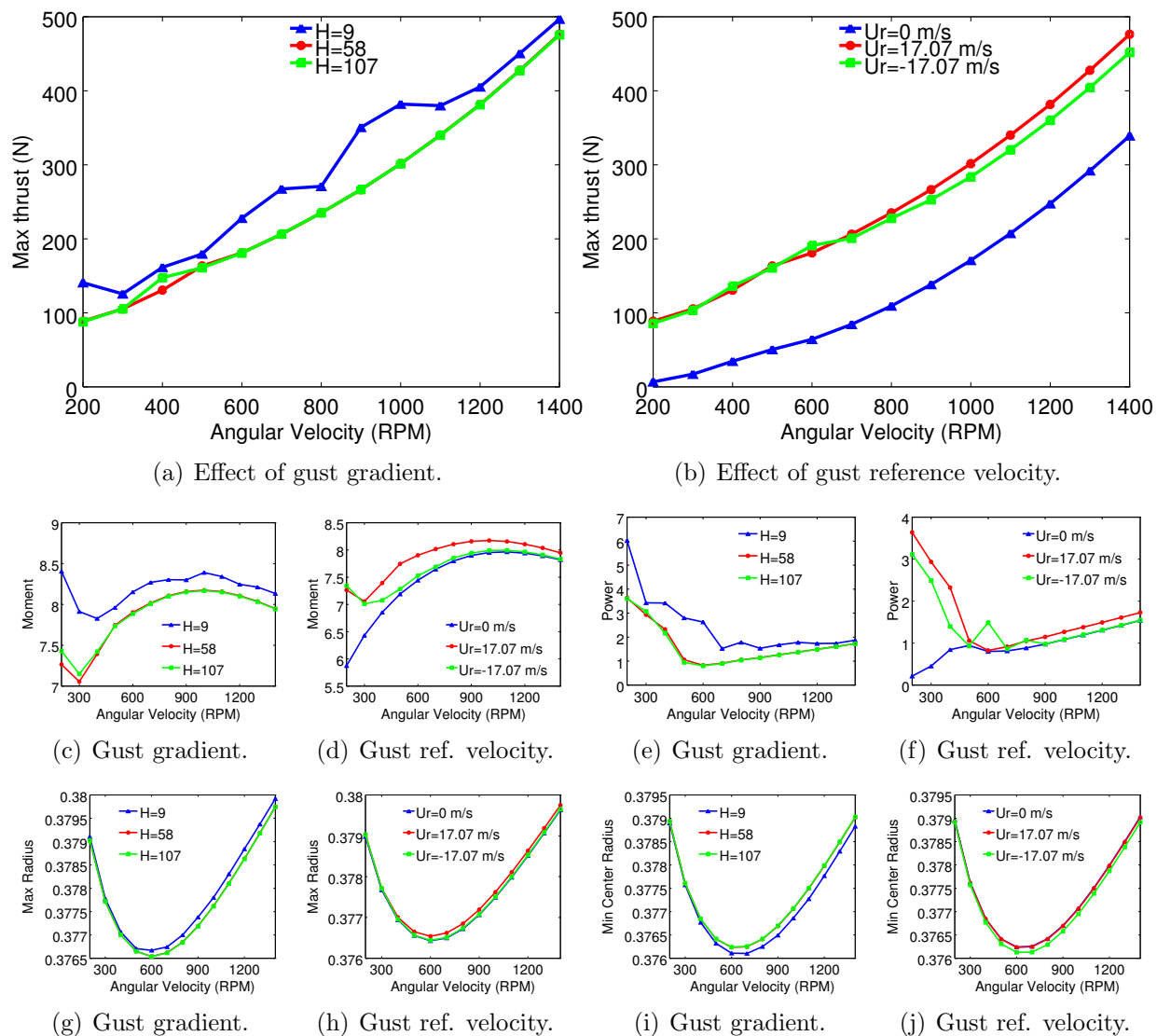(i) Gust gradient.

(j) Gust ref. velocity.

Figure 18. Effect of gust gradients and reference velocities.

The time histories of both slow and fast rotors were observed under the effect of a strong gust having the maximum strength required by EASA and reported earlier in this paper. The velocities were 200 rpm and 1400 rpm, respectively. The gust velocity and the rotor response are plotted in Figs 19 and 20. These figures show time histories of thrust magnitudes in steps of 3N and 20N and the rotor power in hW (100W) and 500W. They also give the gust and inflow velocity magnitudes, the local angle of attack of a blade at its center, and the thrust angle of the rotor. The latter is 180° when propelling the rotor and decreases as the thrust pushes the rotor in the positive gust velocity direction. Figure 20 shows gusts identical to

the one of Fig. 19(a), but with (a) an inverted gust direction, thus streaming downwards, and (b) a shorter gust, which has a longitudinal gradient of $H = 7$.
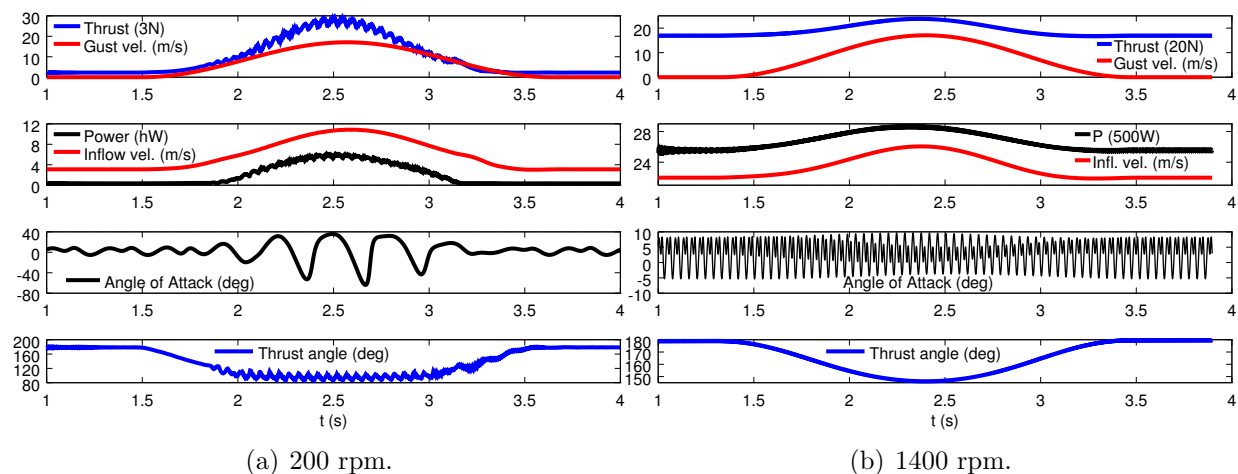

(a) 200 rpm.

(b) 1400 rpm.

Figure 19. Time histories of gust responses.
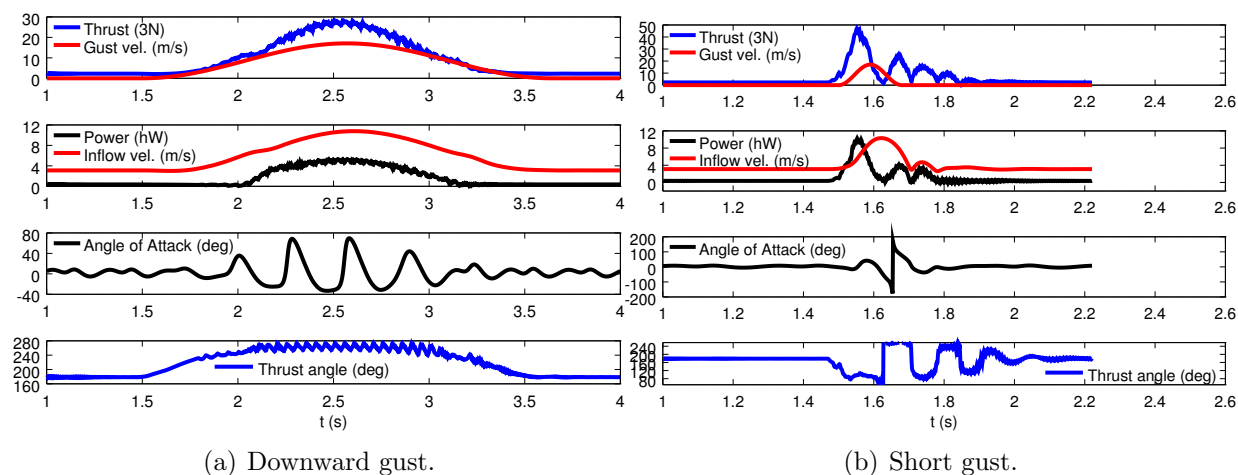

(a) Downward gust.

(b) Short gust.

Figure 20. Time histories of two gusts based on the one plotted in Fig. 19(a).

It is seen that a shorter gust has a much stronger impact than a longer gust of the same velocity. Gusts pushing upwards and downwards are seen to have effects of similar magnitudes on the rotor, but in different directions. The influence on the angle of attack and thrust angle is less pronounced at 1400 rpm than at 200 rpm, but surprisingly the phase between gust and inflow is not smaller. This is explained by the fact that at higher angular velocities the inflow generated by the rotor will be stronger. This is also seen in Figs 17 and 19 which both show smaller ratios of gusty to calm air responses at high angular velocities. For the stiffness considered, the increases and decreases in radius remain small under the disturbance of every gust.

Initially the strongest effect was expected from the gust with the largest gradient H and

reference velocity U_{ref}, since no adaptive changes in the pitching functions is imposed. It however turned out that a shorter gust has a stronger impact on some of the responses. It is suspected that the more erratic behavior of the flow subjected to the gust at lower angular velocities is partly caused by the fewer number of rotor revolutions available to adapt to the gust. This is also confirmed by the fact that the gust with the shorter gradient length of $H = 9$, which means a quicker change in the gusting wind velocity, is the gust which shows the most unstable results at low angular velocities. Another part of the explanation is the weaker induced flow at low rpm. Figure 20(b) highlights the lag in the response of the rotor inflow velocity with respect to the short gust. The cases with the larger longitudinal gradients show a less visible phase lag between the gust and the inflow.

IV.   Conclusions

This work presented the aeroelastic analysis of a cycloidal rotor producing forward thrust. Its blades were thus subjected to steady centrifugal and pulsating aerodynamic loads in the plane of rotation. The performance changes noted by this study mainly come from the impact of the modified blade radius along its span.

An analytical model was used to provide insight into the fundamental behavior of cycloidal rotors and allows preliminary sizing of cycloidal rotor systems. Basic aeroelastic considerations were introduced to understand fundamental aspects of the dynamics of the system. A detailed multibody aeroelastic model was then created to understand how the flexibility of the rotor blades affects the performances. It was calibrated and validated using 3 experimental sources and was also found to agree with the analytical model.

At pitch angles away from stall, more blades means less power required for the same disk loading. Stall is suspected to be very influential on the impact of solidity and the number of blades. The number of blades has a significant influence on thrust and power.

In most cases studied for rigidity, power and thrust generally follow the same trends when away from stall. The multibody model shows that the flexibility of the material and the thickness of the wing skin have important, but different, influences on the strength of the pivot rod. Their differences come from the weight variations caused by the modified skin thickness. One can note that an increase in stiffness causes an increase in required pivot strength. The effects of flexibility on thrust and power are small while those on efficiency are almost null.

The wing gusts have little influence on the required pivot rod strength but an important influence on the maximum rotor power and thrust response and thus potentially on the behavior of the aircraft. The results indicate that a short gust has a stronger and more chaotic influence on the response of the rotor. The angular velocity of the rotor turns out to

have a non-negligible influence on the impact of these short gusts. The direction of the gust has an important impact on the power required and on the direction of the thrust produced. Its impact on the magnitude of the thrust is however negligible. For both upwards and downwards gust, the thrust magnitude increases. The effect on blade deflection caused by the gust is minimal. The lag of the rotor response after the arrival of the gusting wind is minimal regardless of the angular velocity. The lag is nevertheless more pronounced for a short gust.

A solution to avoid the need for strong pivot rods would be to use simply supported blades. In such an arrangement, a further analysis should be conducted because the simply supported blades exhibit a much greater and possibly excessive deformation, as highlighted by the analytical model.

Acknowledgments

References

[1] Heuver, H. M. and Kirsten, K. F. J., "Propeller for aircraft," June 23 1936, US Patent 2,045,233.

[2] Heuver, H. M., "Cycloidal rotor for aircraft," Jan. 1 1952, US Patent 2,580,428.

[3] Darrieus, G. J. M., "Turbine having its rotating shaft transverse to the flow of the current," Dec. 8 1931, US Patent 1,835,018.

[4] Barrass, C., "Chapter 22 - Improvements in propeller performance," *Ship Design and Performance for Masters and Mates*, edited by C. Barrass, Butterworth-Heinemann, Oxford, 2004, pp. 218–227.

[5] Kim, S. J., Yun, C. Y., Kim, D., Yoon, Y., and Park, I., "Design and performance tests of cycloidal propulsion systems," *44th AIAA/ASME/ASCE/AHS/ASC Structures, Structural Dynamics, and Materials Conference*, Norfolk, Virginia, April 7–10 2003, AIAA-2003-1786.

[6] Siegel, S., Seidel, J., Cohen, K., and McLaughlin, T., "A Cycloidal Propeller Using Dynamic Lift," *AIAA 37th Fluid Dynamics Conference and Exhibit*, Miami, FL, June 25–28 2007, Paper AIAA-2007-4232.

[7] Ilieva, G., Páscoa, J. C., Dumas, A., and Trancossi, M., "A critical review of propulsion concepts for modern airships," *Central European Journal of Engineering*, Vol. 2, No. 2, 2012, pp. 189–200, doi:10.2478/s13531-011-0070-1.

[8] Gibbens, R., Boschma, J., and Sullivan, C., "Construction and Testing of a New Aircraft Cycloidal Propeller," *AIAA 13th Lighter-Than-Air Systems Technology Conference Proceedings*, Norfolk, VA, June 28–July 1 1999, Paper AIAA-1999-3906.

[9] Parsons, E., *Investigation and Characterization of a Cycloidal Rotor for Application to a Micro-Air Vehicle*, Master's thesis, 2005.

[10] Benedict, M., Ramasamy, M., Chopra, I., and Leishman, J. G., "Experiments on the Optimization of MAV-Scale Cycloidal Rotor Characteristics Towards Improving Their Aerodynamic Performance," *American Helicopter Society International Specialist Meeting on Unmanned Rotorcraft*, Phoenix, Arizona, January 20–22 2009.

[11] Benedict, M., Ramasamy, M., Chopra, I., and Leishman, J. G., "Performance of a Cycloidal Rotor Concept for Micro Air Vehicle Applications," *Journal of the American Helicopter Society*, Vol. 55, No. 2, 2010, pp. 022002–1–14, doi:10.4050/JAHS.55.022002.

[12] Benedict, M., Mattaboni, M., Chopra, I., and Masarati, P., "Aeroelastic Analysis of a Micro-Air-Vehicle-Scale Cycloidal Rotor," *AIAA Journal*, Vol. 49, No. 11, 2011, pp. 2430–2443, doi:10.2514/1.J050756.

[13] Lind, A., Jarugumilli, T., Benedict, M., Lakshminarayan, V., Jones, A., and Chopra, I., "Flow field studies on a micro-air-vehicle-scale cycloidal rotor in forward flight," *Experiments in Fluids*, Vol. 55, No. 12, 2014.

[14] Yu, H., Bin, L. K., and Rong, H. W., "The research on the performance of cyclogyro," *6th AIAA Aviation Technology, Integration and Operations Conference (ATIO)*, Wichita, Kansas, September 25–27 2006, AIAA 2006-7704.

[15] Du, F. and Hu, Y., *The simulation and analysis of the Roll Stability of the Three-rotor Cyclogyro*, AIAA Aviation, American Institute of Aeronautics and Astronautics, aug 2013, doi:10.2514/6.2013-4219.

[16] Benedict, M., Jarugumilli, T., Lakshminarayan, V., and Chopra, I., "Effect of Flow Curvature on Forward Flight Performance of a Micro-Air-Vehicle-Scale Cycloidal-Rotor," *AIAA Journal*, 2014, pp. 1–11, doi:10.2514/1.J052065.

[17] Shrestha, E., Hrishikeshavan, V., Benedict, M., Yeo, D., and Chopra, I., "Development of Control Strategies and Flight Testing of a Twin-Cyclocopter in Forward Flight," *AHS 70th Annual Forum and Technology Display*, Montreal, Canada, May 20–22 2014.

[18] Altmikus, A. and Bebesel, M., "Helicopter with cycloidal rotor system," June 5 2013, EP Patent 2,511,177.

[19] Hwang, I. S., Lee, H. Y., and Kim, S. J., "Optimization of cycloidal water turbine and the performance improvement by individual blade control," *Applied Energy*, Vol. 86, No. 9, 2009, pp. 1532–1540.

[20] Gagnon, L., Morandini, M., Quaranta, G., Bindolino, G., and Masarati, P., "Cyclogyro Thrust Vectoring for Anti-Torque and Control of Helicopters," *AHS 70th Annual Forum and Technology Display*, Montreal, Canada, May 20–22 2014.

[21] Benedict, M., Jarugumilli, T., and Chopra, I., "Effect of Rotor Geometry and Blade Kinematics on Cycloidal Rotor Hover Performance," *Journal of Aircraft*, Vol. 50, No. 5, 2013, pp. 1340–1352, doi:10.2514/1.C031461.

[22] Yun, C. Y., Park, I. K., Lee, H. Y., Jung, J. S., and Hwang, I. S., "Design of a New Unmanned Aerial Vehicle Cyclocopter," *Journal of the American Helicopter Society*, Vol. 52, No. 1, 2007, pp. 24–35, doi:10.4050/JAHS.52.24.

[23] Johnson, W., *Helicopter Theory*, Dover Publications, New York, 1994.

[24] Xisto, C. M., Páscoa, J. A., Leger, P., Masarati, P., Quaranta, G., Morandini, M., Gagnon, L., Wills, D., and Schwaiger, M., "Numerical modelling of geometrical effects in the performance of a cycloidal rotor," *11th World Conference on Computational Mechanics*, Barcelona, Spain, July 20–25 2014.

[25] McNabb, M. L., *Development of a Cycloidal Propulsion Computer Model and Comparison with Experiment*, Master's thesis, 2001.

[26] Ghiringhelli, G. L., Masarati, P., and Mantegazza, P., "A Multibody Implementation of Finite Volume C Beams," *AIAA Journal*, Vol. 38, No. 1, January 2000, pp. 131–138, doi:10.2514/2.933.

[27] Yang, K., *Aerodynamic analysis of an MAV-scale cycloidal rotor system using a structured overset RANS solver*, Master's thesis, University of Maryland at College Park, 2010.

[28] Young, W., Budynas, R., and Sadegh, A., *Roark's Formulas for Stress and Strain*, McGraw Hill, 2011.

[29] Gagnon, L., Morandini, M., Quaranta, G., Muscarello, V., and Masarati, P., "Aerodynamic models for cycloidal rotor analysis," *Aircraft Engineering and Aerospace Technology: An International Journal*, Vol. 88, No. 2, 2016, pp. 215 – 231.

[30] European Aviation Safety Agency, "Certification Specifications and Acceptable Means of Compliance for Large Aeroplanes CS-25 / Amendment 15," Tech. rep., European Aviation Safety Agency, 2014.